



Available online at [www.sciencedirect.com](http://www.sciencedirect.com)

**jmr&t**  
Journal of Materials Research and Technology

journal homepage: [www.elsevier.com/locate/jmrt](http://www.elsevier.com/locate/jmrt)



## Original Article

# Influence of expulsion and heat extraction resulting from changes to electrode force on liquid metal embrittlement during resistance spot welding



S. Song <sup>a,\*</sup>, M. Shojaee <sup>a</sup>, A.R.H. Midawi <sup>a</sup>, O. Sherepenko <sup>a</sup>,  
Hassan Ghassemi-Armaki <sup>b</sup>, E. Biro <sup>a</sup>

<sup>a</sup> Department of Mechanical and Mechatronics Engineering, University of Waterloo, Waterloo, Canada

<sup>b</sup> General Motors R&D, Manufacturing Systems Research Laboratory, Warren, MI, 48092, USA

### ARTICLE INFO

#### Article history:

Received 11 November 2022

Accepted 14 January 2023

Available online 22 January 2023

#### Keywords:

Resistance spot welding (RSW)

3G advanced high-strength steels  
(3G-AHSS)

Liquid metal embrittlement (LME)

Electrode force

Expulsion

Heat extraction

### ABSTRACT

Zinc coatings are generally utilized for manufacturing corrosion-resistant advanced high-strength steels (AHSS). However, in new third generation AHSS (3G-AHSS), zinc from the coating may interact with the steel substrate leading to liquid metal embrittlement (LME) cracking during resistance spot welding (RSW). A critical RSW parameter that influences the LME response of the utilized 3G-AHSS is the electrode force. This study showed that the influence of electrode force on LME depended on whether or not welds experienced expulsion. When welding with low heat input, without expulsion, LME cracking severity decreased as electrode force increased. In such cases, increased force aided with heat extraction during welding, relieving the critical stresses required by LME cracking. In contrast, when welding with high heat input, resulting in expulsion, increased force elevated LME cracking. It was shown that high force increased the sudden indentation of the electrode into the substrate (electrode collapse), leading to rapid cooling of the weld shoulder. The rapid cooling increased the thermal stresses associated with the collapse event, promoting LME. This study established that the electrode force has two distinct roles on LME. When welding below the expulsion current, high force decreased LME. On the other hand, when welding above the expulsion current, more severe LME cracking was observed at high electrode force. The results from this study show that expulsion itself (excluding its association with increased heat input) is a factor contributing to LME cracking, which highlights the importance of considering the expulsion phenomenon in designing LME resistant welding schedules.

© 2023 The Author(s). Published by Elsevier B.V. This is an open access article under the CC BY license (<http://creativecommons.org/licenses/by/4.0/>).

\* Corresponding author.

E-mail address: [s83song@uwaterloo.ca](mailto:s83song@uwaterloo.ca) (S. Song).

<https://doi.org/10.1016/j.jmrt.2023.01.093>

2238-7854/© 2023 The Author(s). Published by Elsevier B.V. This is an open access article under the CC BY license (<http://creativecommons.org/licenses/by/4.0/>).

<b>Nomenclature</b>		
AHSS	Advanced high-strength steels	CI A Crack index counting only Type A cracks
1G-AHSS	First generation AHSS	CI B Crack index counting only Type B cracks
2G-AHSS	Second generation AHSS	CI C Crack index counting only Type C cracks
3G-AHSS	Third generation AHSS	n Number of cracks per weld
GI	Galvanized	L Lognormal median crack length
GA	Galvannealed	ts Sheet thickness
EG	Electro-plating	dt Change of welding time
RSW	Resistance spot welding	t0 Start time of welding cycle
LME	Liquid metal embrittlement	t1 Finish time of welding cycle
UTS	Ultimate tensile strength	I Welding current
YS	Yield strength	R Electrical resistance
EI	Elongation	Qw Total heat input during the RSW process
CEY	Carbon equivalent calculated by the formula from Yurioka et al.	Ql Heat loss (Heat extraction)
MFDC	Medium-frequency direct current	Qm Heat required to melt the material which ultimately solidifies to a weld nugget
I <sub>max-10%</sub>	Low heat input (Weld nugget diameter equivalent to the baseline condition with ten percent below expulsion current)	m Nugget mass
I <sub>max-200 A</sub>	Moderate heat input (Weld nugget diameter equivalent to the baseline condition with 200 A below expulsion current)	T Temperature
I <sub>max+10%</sub>	High heat input (Weld nugget diameter equivalent to the baseline condition with ten percent above expulsion current)	dT Change of temperature
Type A cracks	LME cracks locate at the weld indent	T <sub>m</sub> Melting temperature
Type B cracks	LME cracks locate at the weld shoulder extending to the edge of the heat affected zone	RT Room temperature
Type C cracks	LME cracks locate at the weld notch	C <sub>p</sub> Specific heat capacity of steel
CI	Crack index	u Nugget volume
CI T or Total CI	Crack index counting all Type A, B and C cracks	d Nugget diameter
		h Nugget height
		$\rho$ Steel density
		F <sub>electrode</sub> Electrode force
		P Ferrostatic pressure
		LB Before expulsion with low electrode force
		LA After expulsion with low electrode force
		HB Before expulsion with high electrode force
		HA After expulsion with high electrode force

## 1. Introduction

New emission standards require increased fuel economy for new light-duty vehicles compared to current vehicles on the market [1]. For example, the amount of permitted CO<sub>2</sub> emission for new light vehicles is predicted to decline to the extend that there will be a reduction of more than three billion tons of greenhouse gas emissions by 2050 [2]. One of the ways that the automotive industry will achieve this goal is by reducing autobody weight by decreasing the material thickness of steels used for body-in-white construction [2]. Advanced high-strength steels (AHSS) have higher ductility than similar strength conventional steels, so they can be used to make thinner parts without compromising vehicle safety; approximately 40% to 50% of body structure of a modern vehicle is made of AHSS [3]. Three generations of AHSS have so far been designed; these are classified by functional microstructural constituents with the third generation AHSS (3G-AHSS) being the latest one. 3G-AHSS have enhanced formability, when compared to similar strength first generation AHSS (1G-AHSS), and use fewer alloying elements, have reduced

manufacturing costs, and improved weldability compared to second generation AHSS (2G-AHSS) [3,4]. Zinc coating is applied to the surface of AHSS for resisting corrosion by typical methods of hot-dipping (galvanized (GI), galvannealed (GA) or electro-plating (EG) [5].

Resistance spot welding (RSW) is the dominant welding technique for the body-in-white assembly. During the RSW process the sheets to be joined are fitted together in a lap-joint configuration. They are then clamped by water-cooled copper electrodes. The clamping force from the electrodes is exerted throughout the welding cycle. After clamping, welding current passes through the joint and the sheets are fused together by the generated heat with the current flow. Then, the welding current is terminated and the electrodes extract remaining heat from the weld to solidify the molten nugget [6]. During the welding process, the temperature at the sheet surface will exceed zinc melting temperature of 419 °C. If there is sufficient stress, the liquid zinc will act as an embrittling agent, causing liquid metal embrittlement (LME) cracking, possibly degrading weld strength [7].

Previous research into LME cracking have shown that welding parameters and boundary conditions, such as

electrode geometry [8–11], electrode force [12–17], welding current [13,18,19], and hold time [20] influenced the severity of LME cracking due to their ability to influence temperature, stress, and morphology evolution in the welding area. In addition, LME suppression can be achieved through use of radius-type electrodes [8], larger electrode tip area [9,10], pre-pulsing [13], multi-pulsing [18,21], ramping profile current [19], and prolonged hold time [22]. The body of literature, describing the influence of electrode force on LME cracking, showed a linear decrease in LME severity of LME cracking as electrode force increased, which the authors attributed the decrease in LME cracking causing by heat transfer as electrode force increased [12,13,15,17]. It should be noted though that except for Choi et al.'s study, none of other electrode force studies compensated for how changing electrode force influence heat generation during welding, resulting in welds made with various electrode forces forming different sized nuggets (with differing associated thermal and stress fields). Furthermore, previous studies investigating how electrode force impacts LME cracking were conducted at heat input levels below the expulsion limit. Considering the frequency of expulsion during automotive assembly, the impact of electrode force on LME at heat levels sufficient to cause expulsion is required.

In the present work, the effect of electrode force on LME cracking was examined with low, moderate and high heat input levels. The welding current was adjusted accordingly with the electrode force to compensate for changes to heat input. Cracking severity resulting from the welding conditions was characterized using a quantitative metric, the crack index. The behavior of LME cracking, associated with the electrode force variation, was explained with respect to the thermal contact between the electrode and the metal sheet, and the electrode collapse. This research also provides insights into impact of expulsion on LME cracking severity.

## 2. Materials and methods

### 2.1. Materials

This study was carried using a 1.4 mm thick hot-dipped galvanized 3G-AHSS with an ultimate tensile strength (UTS) of 1015 MPa. The material was known to be LME-sensitive. The carbon equivalent (CEY) and mechanical properties: ultimate tensile strength (UTS), yield strength (YS), and total elongation (total EI), of the investigated material can be found in Table 1. The carbon equivalent (CEY) was calculated according to the formula from Yurioka et al. [23].

### 2.2. Welding

All welding in this study was performed on two-high homogenous joints using a 125 kVA medium-frequency direct current (MFDC) robotic spot welder timed by Bosch Rexroth controller. The system was capable of a maximum electrode force of 5.5 kN, applied by a servo electric mechanical system. The industrial C-type welding gun was used and positioned by a Fanuc robotic arm. Resistance Welding Manufacturing Alliance (RWMA) 5/8" Type B, dome-shaped electrodes with a face diameter of 7 mm and a flat contact face were used, as shown

**Table 1 – Carbon equivalent and mechanical properties of the investigated material.**

CEY	Mechanical Properties		
	YS (MPa)	UTS (MPa)	Total EI (%)
0.657	634 ± 8	1015 ± 6	19.9 ± 0.8

in Fig. 1. The electrodes were water-cooled with 6 L/min flow rate. The modified electrode force conditions of 4.4 kN and 5.4 kN shared same welding schedule with the baseline 4.9 kN electrode force condition, which can be found in Table 2. The baseline welding schedule complied with the American Welding Society (AWS) D8.9M [24] recommendation, leading to a dual-pulse welding current schedule where each current pulse was 167 ms long separated by a 33 ms cooling time.

Before welding, electrodes were dressed by a tip dresser, and then electrodes were stabilized by making 24 welds using the AWS D8.9 M baseline welding schedule with a 9.9 kA stabilization current. The welding current range was determined using the AWS D8.9M procedure. The baseline welding current were defined using an electrode force of 4.9 kN where the different heat input levels were defined relative to the measured expulsion current ( $I_{max}$ ) of 10.8 kA. Welds were made using with low heat input ( $I_{max}-10\%$ ), moderate heat input ( $I_{max}-200\text{ A}$ ), and high heat input ( $I_{max}+10\%$ ). As electrode force variation changes the amount of heat generated during welding [12], welding currents for a low electrode force (4.4 kN) and high electrode force (5.4 kN) were adjusted to match the nugget size of the baseline force condition (4.9 kN). In other words, the amount of heat generated during nugget formation was kept constant with respect to each heat input

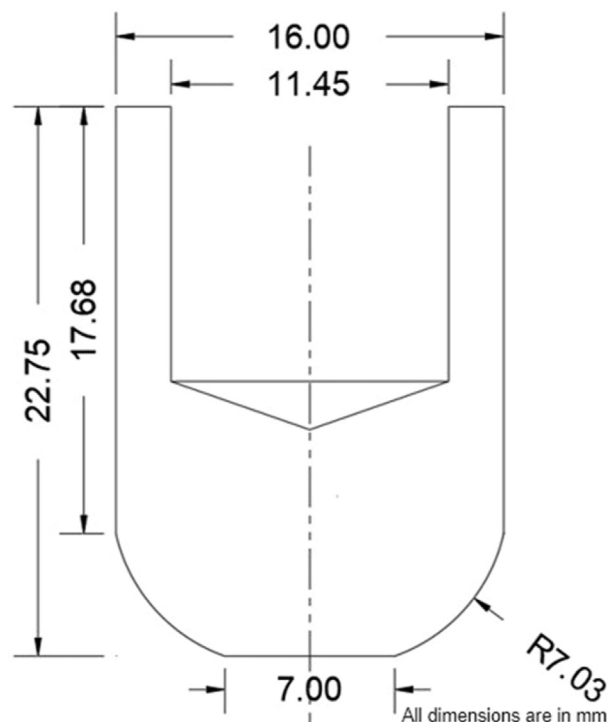


**Fig. 1 – RWMA 5/8" Type B, dome-shaped electrode with 7 mm face diameter [25].**

**Table 2 – Resistance spot welding parameters [24].**

Electrode Force (kN)	Squeeze Time (ms)	Pulse Schedule (ms)	Hold Time (ms)
4.4	167	167-33-167	167
4.9 (Baseline)			
5.4			

level for all three electrode forces. So, for example, although high heat input welds are noted as  $I_{max}+10\%$ , welding current was still varied appropriately so that the welds made at 4.4 kN, 4.9 kN and 5.4 kN electrode forces all had same nugget diameter as the  $I_{max}+10\%$  baseline condition of 4.9 kN. The welding currents and nugget diameters used for all welding conditions can be seen in **Table 3**. Five welds were made per condition for LME cracking analysis. **Fig. 2** depicts nugget diameter, nugget height and indent depth viewing from the weld cross-section. The indent depth was calculated by the difference between the sheet thickness and half of the total thickness of the indentation region of the joint as measured from the metallographic cross-section of the weld.

### 2.3. Qualification of LME cracking severity

The distribution of LME cracks was viewed from the weld cross-section as defined by the cutting plane passing through the weld center and crossing most severe visible surface cracks as described by DiGiovanni et al. [26]. The cross-sectioned welds were then hot mounted and polished using standard metallographic methods to a 1  $\mu\text{m}$  diamond final polish. Crack locations were described as per Choi et al.'s [12] classification which divided cracked regions as: the electrode indent of the weld (Type A crack), shoulder of the weld and extending to the edge of the heat affected zone (Type B crack), and the weld notch (Type C crack). The quantity and length of Type A, B, and C cracks (see **Fig. 3**) were measured on the unetched surface using a Carl ZEISS Axio Vert. A1 optical microscope at magnifications of 200x. The crack length was defined as the straight-line distance from the cracking opening at the zinc coating side to the crack tip. The cracking severity was characterized as per crack index (CI), developed by Wintjes et al. [27], was used to quantify LME cracking severity Eq. (1).

$$CI = \frac{nL}{t_s} \quad (1)$$

Where  $n$  is the number of cracks per weld,  $L$  is the lognormal median crack length, and  $t_s$  is the sheet thickness. The crack index can be thought as a ratio of the total length of cracks in the weld cross-section to the sheet thickness and explains the strength loss caused by LME cracks. The error bars shown on graphs indicate the 95% confidence interval of the data.

### 2.4. Investigation on heat generation and heat extraction during the RSW process

The total heat input ( $Q_w$ ) during the RSW process was calculated by the Joules' law as per Eq. (2) below [6]:

Table 3 – The selection of welding current with altering electrode force at various heat input levels.			
Heat Input Levels	$I_{max}-10\%$ (Low heat input)	$I_{max}-200\text{ A}$ (Moderate heat input)	$I_{max}+10\%$ (High heat input)
Parameters	Welding current (kA)	Average nugget diameter (mm)	Average nugget diameter (mm)
Electrode force			
Baseline electrode force (4.9 kN)	9.7	10.6	11.9
Increased electrode force (5.4 kN)	9.8	11.4	12.1
Decreased electrode force (4.4 kN)	9.6	10.7	11.4
			7.4

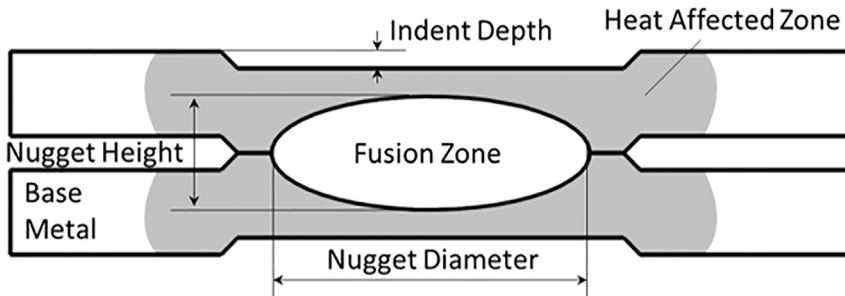


**Fig. 2 – Schematic showing nugget diameter, nugget height and indent depth from the weld cross-section.**

$$Q_w = \int_{t_0}^{t_1} I^2 \cdot R \cdot dt \quad (2)$$

Where  $t_0$ ,  $t_1$ ,  $I$ ,  $R$  and  $dt$  denote start time of welding cycle, finish time of welding cycle, welding current, electrical resistance, and change of welding time, respectively. The electrical resistance was calculated by dividing the instantaneous voltage by the current. A data acquiring system, connected to the controller, recorded the instantaneous welding current and voltage at a frequency on 1 kHz.

The heat loss ( $Q_l$ ) was defined as a difference between the total heat input ( $Q_w$ ) and melting heat ( $Q_m$ ) in Eqs. (3) below [6]:

$$Q_l = Q_w - Q_m \quad (3)$$

$Q_m$  is the calculated heat required to melt the material which ultimately solidifies to a weld nugget. It was calculated as below [6]:

$$Q_m = m \cdot \int_{RT}^{T_m} Cp(T) dT \quad (4)$$

Where  $m$  is nugget mass,  $Cp$  is specific heat capacity of steel, as calculated using JMatPro 12.4.  $T_m$  and  $RT$  are the melting temperature and the room temperature, respectively. It was assumed that the weld nugget was ovoid in shape to estimate the nugget mass ( $m$ ) as derived from Eqs. 5 and 6 below since only ordinary nugget shape was observed from the cross-sectional views of welds [6]:

$$u = \frac{4}{3} \pi \cdot \frac{d^2}{4} \cdot \frac{h}{2} \quad (5)$$

$$m = u \cdot \rho \quad (6)$$

Where  $d$  and  $h$  are nugget diameter and nugget height, respectively, depicted in Fig. 2  $u$  is the nugget volume and  $\rho$  is the steel density ( $7.85 \times 10^{-3}$  g/mm $^3$ ). Micrograph images of the weld cross-sections were taken using an automated Clemex CMT microscope. Carl Zeiss Blue software package was used to measure the nugget height and diameter from the weld cross-sections.

### 3. Results and discussion

#### 3.1. Correlation of LME cracking severity with electrode force variation

In the present study, welds were made at the low ( $I_{max}-10\%$ ), moderate ( $I_{max}-200$  A) and high ( $I_{max}+10\%$ ) heat inputs, and their corresponding LME severity (see Fig. 4) and crack distribution (see Figs. 5–7) are interpreted as following. At low heat input level, only Type B cracks were detected (see Fig. 4) and the increase of electrode force led to a reduction of both the number and length of cracks (see Fig. 5), which agrees with the literature [12]. At moderate heat input level, both Type A and Type B cracks were observed (see Fig. 4). When electrode was increased from 4.4 kN to 4.9 kN, the number of Type A cracks decreased from 32 cracks to 1 crack, the number of A Type cracks increased to 15 cracks when electrode force was further increased to 5.4 kN. The maximum Type A crack length increased linearly from 389.6  $\mu$ m with an electrode force of 4.4 kN to 854.2  $\mu$ m with 5.4 kN of electrode force (see Fig. 6). The number of Type B cracks decreased from 69 cracks when welding with an electrode force of 4.4 kN to 37 cracks with using 4.9 kN of electrode force and then increased to 66 cracks with 5.4 kN of electrode force. The maximum crack length of Type B cracks increased from 250.1  $\mu$ m when 4.4 kN electrode force was used to 284.4  $\mu$ m with an electrode force of 4.9 kN and then decreased again to 93.1  $\mu$ m with an electrode force of 5.4 kN (see Fig. 6). At high heat input level, the number of Type A cracks increased from 14 to 31 with an increase in maximum crack length from 755.3  $\mu$ m to 818.6  $\mu$ m when the electrode force was increased from 4.4 kN to 5.4 kN (see Fig. 7). Furthermore, the quantities and maximum crack length of Type B cracks increased when the electrode force was

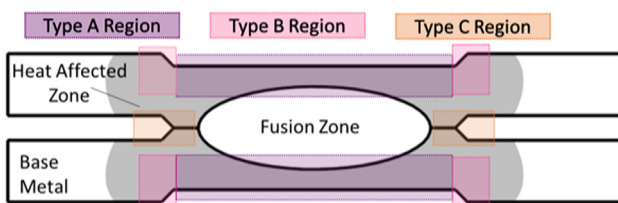


**Fig. 3 – Schematic of different types of LME cracks viewing from the weld cross-section.**

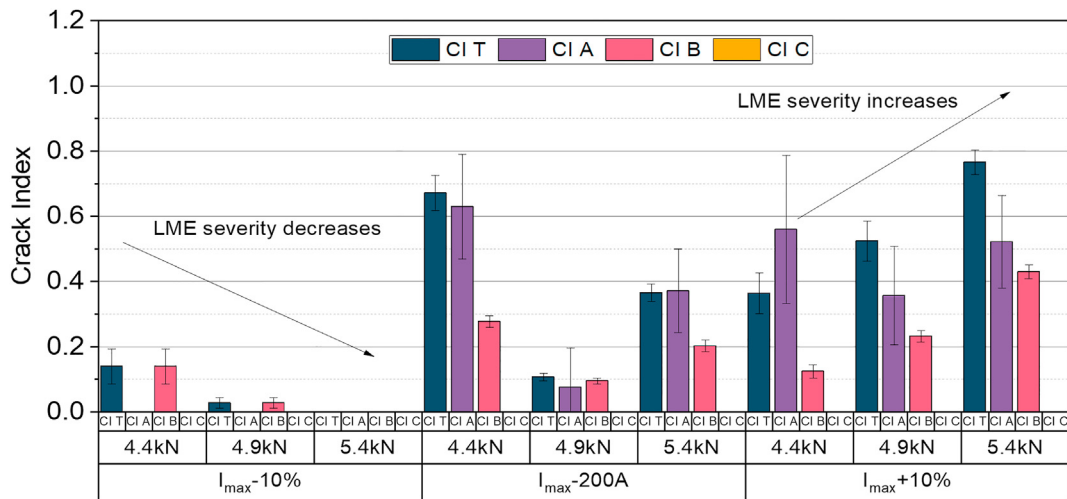


**Fig. 4 – Crack Index of Total and Individual Type crack at various heat input levels with 4.4 kN, 4.9 kN and 5.4 kN electrode forces; CI T is crack index calculated from all cracking data (Type A, B and C cracks); CI A is crack index calculated for Type A cracks; CI B is crack index calculated for Type B cracks; CI C is crack index calculated for Type C cracks.**

increased from 4.4 kN (32 cracks, 159.6  $\mu\text{m}$ ) to 5.4 kN (129 cracks, 165.9  $\mu\text{m}$ ).

When LME cracking severity was quantified using the crack index the influence of electrode force on LME cracking could be seen clearer (see Fig. 4). At low heat input, only Type B cracks were observed, so the Total crack index (the crack index calculated from all cracking data regardless of location) and the crack index of Type B cracks were equal. The LME cracking severity decreased with the increase of electrode force. At moderate heat input, there was no correlation between the electrode force level and the LME cracking severity. However, the largest Total crack index, as well as contributions from Type A and Type B cracks were seen at the lowest electrode force (4.4 kN) level and decreased when electrode force was increased from 4.4 kN to 4.9 kN; LME cracking severity then increased when electrode force was increased from 4.9 kN to 5.4 kN. At high heat input, there was no significant effect of electrode force on Type A cracking severity. However, both Total and Type B crack indexes increased linearly with the increase of electrode force from 4.4 kN to 5.4 kN.

From the present observations, at moderate and high heat input levels, the increase of electrode force did not cause a linear reduction of LME cracking, which contradicts the literature [12,13,15,17].

### 3.2. Correlation of LME cracking with heat extraction

The interaction effects of heat input (represented by welding current) and electrode force on LME cracking was summarized in Fig. 8a by DiGiovanni et al. [17]. The study showed that increasing heat input increased LME cracking severity, but high electrode force could mitigate LME cracking, even when the heat input was high. It is worth mentioning that welding current was not adjusted to compensate for the effect of changing electrode force in that work. In the present study, the effect of electrode force on LME cracking diverged from the conclusions within the literature as it was observed that, at moderate and high heat input levels, LME did not decrease with increased electrode force (see Fig. 8b). Although, it should be noted that at low heat input, LME cracking decreased with

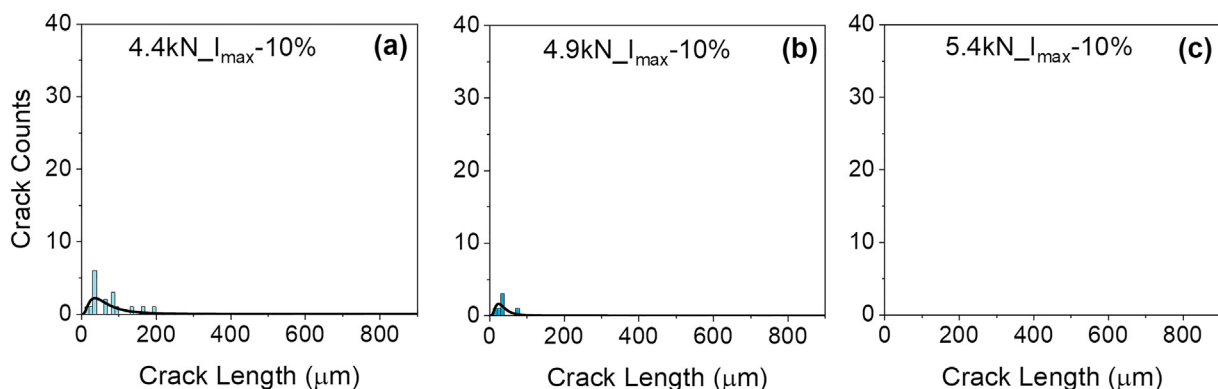


**Fig. 5 – Total crack distribution at low heat input level (I<sub>max</sub>-10%) with (a) 4.4 kN; (b) 4.9 kN; (c) 5.4 kN.**

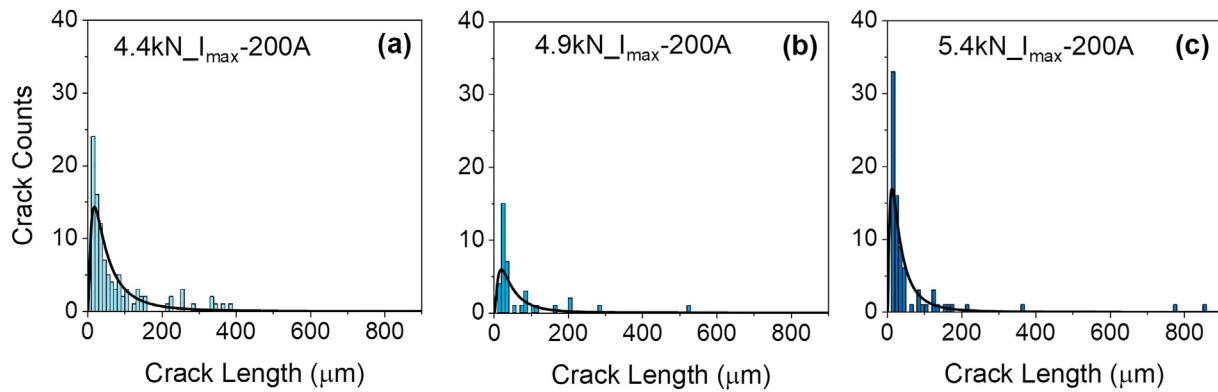


**Fig. 6 – Total crack distribution at moderate heat input level ( $I_{\max}$ -200 A) with (a) 4.4 kN; (b) 4.9 kN; (c) 5.4 kN.**

increased of electrode force, in-line with the literature [12,13,15,17]. At moderate heat input, welds with both low electrode force and high electrode force experienced high LME cracking. At high heat input, LME cracking increased as electrode force was increased.

The heat map in Fig. 9 correlates heat loss with electrode force at various heat input levels of the present work. At all heat input levels (low, moderate and high), heat loss increased with the increase of electrode force. This link between electrode force and heat loss is due to the electrode contact area enlarging as electrode force increases. The increase in contact improves the cooling effect i.e. larger amount of heat loss by increasing area and decreasing contact resistance [8,12]. At low heat input, increased heat loss mitigated LME cracking. However, increasing heat loss did not reduce LME cracking in welds made with moderate and high heat input. Therefore, there should be another dominant factor influencing the severity of LME cracking aside from heat loss at these heat input levels. This will be further discussed in the following section.

### 3.3. Correlation of LME cracking with electrode collapse and expulsion

High LME cracking has been seen in welds that experienced expulsion [28]. Although the explicit link between expulsion

and LME cracking has not been made, it may contribute to LME formation, separate to the contribution from increasing heat input. The investigation of the influence of expulsion on LME cracking was characterized by counting the number of welds in each group of five, made with the same welding parameters, that exhibited an expulsion event. Expulsion events were determined by examining the dynamic resistivity curves calculated from the instantaneous voltage and current data measured by the weld timer during each welding cycle. Expulsion was identified by the sharp decrease of resistance on the dynamic resistivity curve. Whether or not a particular welding condition produced expulsion was determined by how many welds of the five made at each condition experienced expulsion. Zero, three, four and five expulsions were detected within per five welds. Conditions that produced no welds with expulsion were denoted as the “No Expulsion” condition, and welds where the majority of the welds (3, 4, or 5 welds) experienced expulsion were denoted as the “Yes Expulsion” condition (see Fig. 10). Expulsion was not observed for any of the conditions made with low heat input. In these welds, the increase in electrode force enhanced cooling effect and reduced LME cracking, as described by literature [12,13,15,17]. At the moderate heat input level, LME formation was decoupled from heat extraction. It was seen that LME cracking decreased as heat extraction increased when electrode force was increased from 4.4 kN to 4.9 kN. However, it

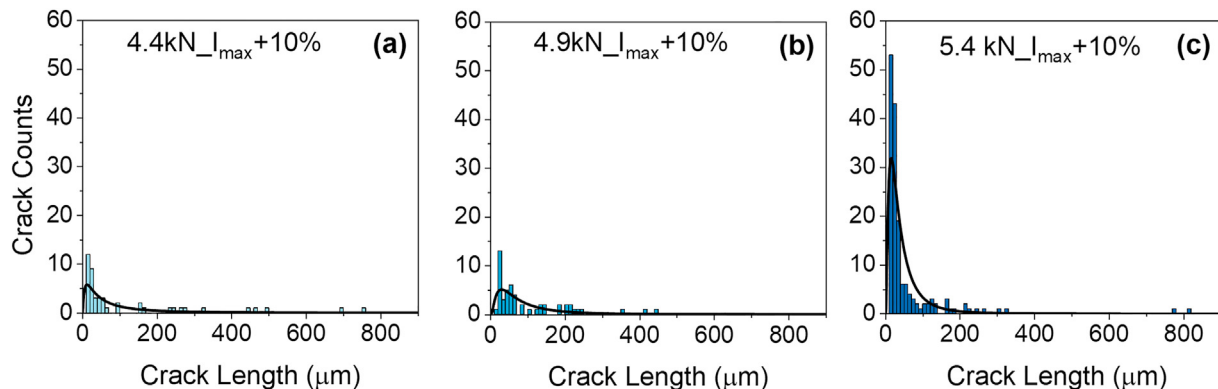


**Fig. 7 – Total crack distribution at high heat input level ( $I_{\max}+10\%$ ) with (a) 4.4 kN; (b) 4.9 kN; (c) 5.4 kN.**

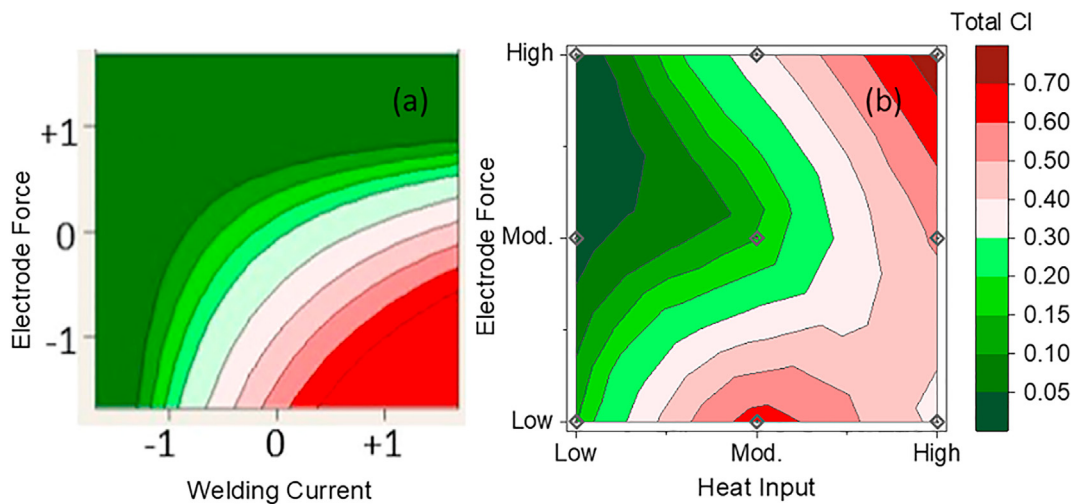


**Fig. 8 – Effects of electrode force on LME cracking at various heat input levels: (a) summary from the literature [17]; (b) observations of the present research; Total CI is the crack index calculated from all cracking data (Type A, B and C cracks).**

was also seen that LME cracking increased with further increases in electrode force to 5.4 kN, even though this further increased heat extraction. Although, it should be noted that the welds made using electrode forces of 4.4 kN and 5.4 kN experienced expulsion, whereas the welds made with an electrode force of 4.9 kN did not. At the high heat input level, expulsion occurred at all electrode force conditions. At this heat input, although increasing electrode force still increased heat loss (see Fig. 9), LME cracking increased with increasing electrode force. These results show that below the expulsion limit, the relation between electrode force and LME cracking is controlled by heat loss to the electrodes, where increasing electrode force, increases heat loss and decreases LME cracking. However, when welding above the expulsion limit, there is another phenomenon that is occurring that exasperates LME cracking with increasing electrode force, which is more influential than heat loss.

In this study, Type B cracks were observed at all heat input levels and the consequence of Type B cracking from electrode force variation aligned with the Total LME cracking behavior (Figs. 4 and 10). It is also clear that the formation of Type B cracks was driven by expulsion occurrence, where welds made with moderate heat input that experience expulsion showed much higher B Type crack severity than the weld that did not experience expulsion, whereas the increase of A Type cracking in welds experiencing expulsion was not as great. It is known that the formation of B Type cracks is due to thermal stress generated from the rapid cooling that occurs when the electrode suddenly sinks into the steel (electrode collapse) as the hot strength of the steel drops on heating [8]. When the weld is expulsion-free, the electrode force is being countered by both the material strength and the ferrostatic pressure of the molten metal, enclosed in the corona bond, so the rate and depth of electrode collapse is purely a function of the material hot strength [20]. However, expulsion disrupts this natural equilibrium influencing electrode position. The schematic in Fig. 11a compares influences of electrode collapse on welds without expulsion (left half) and with expulsion (right half). The effect of expulsion on LME cracking can be divided in mechanical and thermo-mechanical components, acting simultaneously. During expulsion, liquid metal is rapidly lost from the molten nugget. Due to speed of this event, it would be expected that this would lead to a rapid drop in the ferrostatic pressure of nugget, disrupting the mechanical equilibrium between the weld joint and electrodes, affecting the electrode collapse event during the weld cycle. As such, the rapid reduction in counterforce from the nugget against the electrode leads to a sudden electrode collapse and thus fast tensile deformation of the sheet surface [20,29]. Böhne et al. [22] showed that faster deformation can be associated with more LME cracks formation. Increase in collapse deformation rate during expulsion may similarly cause more severe LME cracking [29]. As well, this sudden and deep deformation will increase of contact area between the electrode and the weld

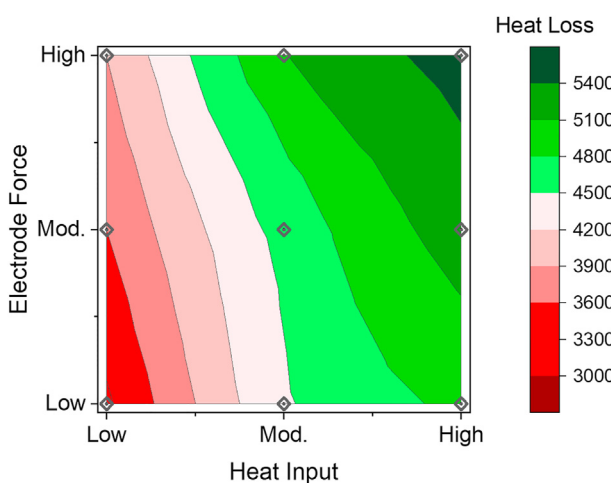


**Fig. 9 – Correlation of electrode force to heat loss at low, moderate, and high heat input levels.**

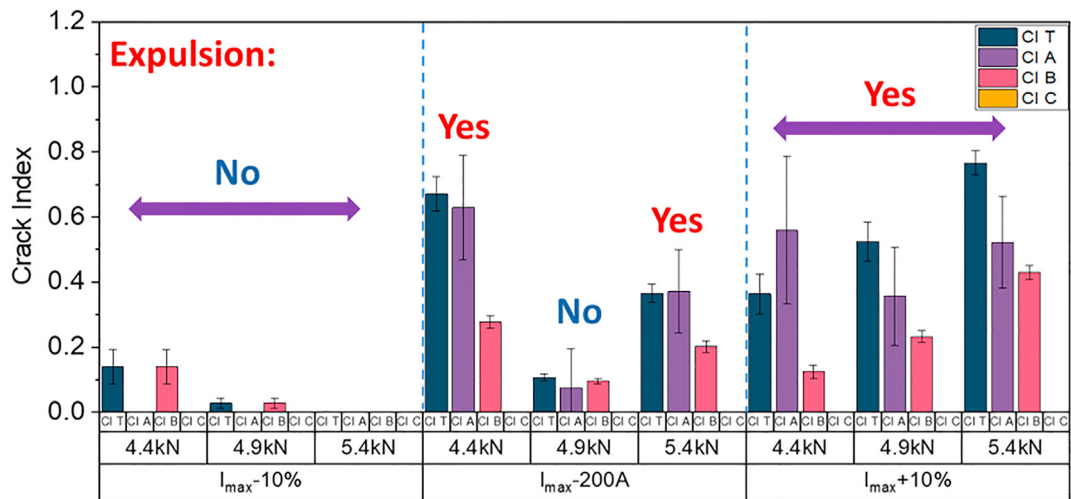


Fig. 10 – No Expulsion case and Yes Expulsion cases among various heat input levels with electrode force variation.

shoulder, greatly enhancing heat extraction, developing more tensile stress at the affected area, which can be described as the “thermo-mechanical” component of the expulsion effect on LME cracking. The effect of expulsion on electrode indent can be visualized by comparing cross-sections of welds with low, moderate and high electrode forces at moderate heat input level, presented in Fig. 11b, c, and d, respectively. At low (4.4 kN) and high (5.4 kN) electrode force levels, welds experienced expulsion and had deeper indents along with more severe LME cracking (see Figs. 4 and 10) than the weld without expulsion at the moderate (4.9 kN) electrode force condition.

The influence of electrode force on expulsion can be described by analyzing the balance of forces acting on the molten metal for two conditions: “low electrode force” and “high electrode force” as shown in Fig. 12. Where  $F_{electrode}$  is the electrode force;  $P$  is the ferrostatic pressure within the nugget to resist the electrode force and maintains nugget morphology; subscripts of (LB, LA) and (HB, HA) mean before and after expulsion for the low electrode force case, and before and after expulsion for the high electrode force case, respectively. Higher electrode force leads to increase in ferrostatic pressure inside the nugget and allows to achieve a stronger corona bond [20]. When the corona bond is breached,

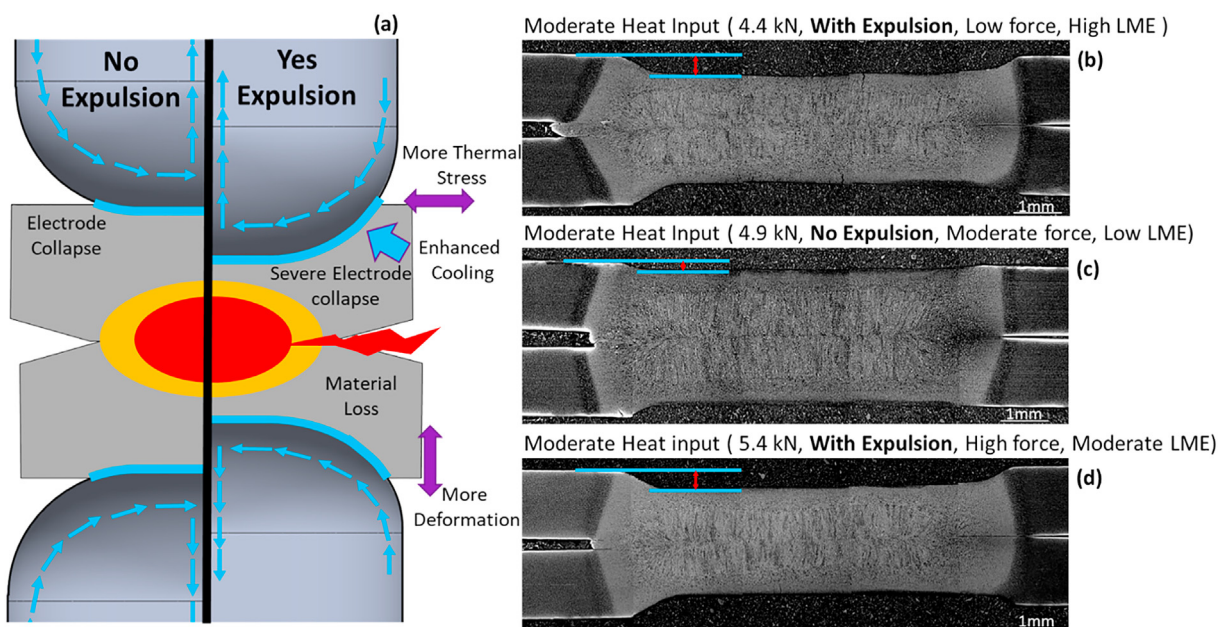
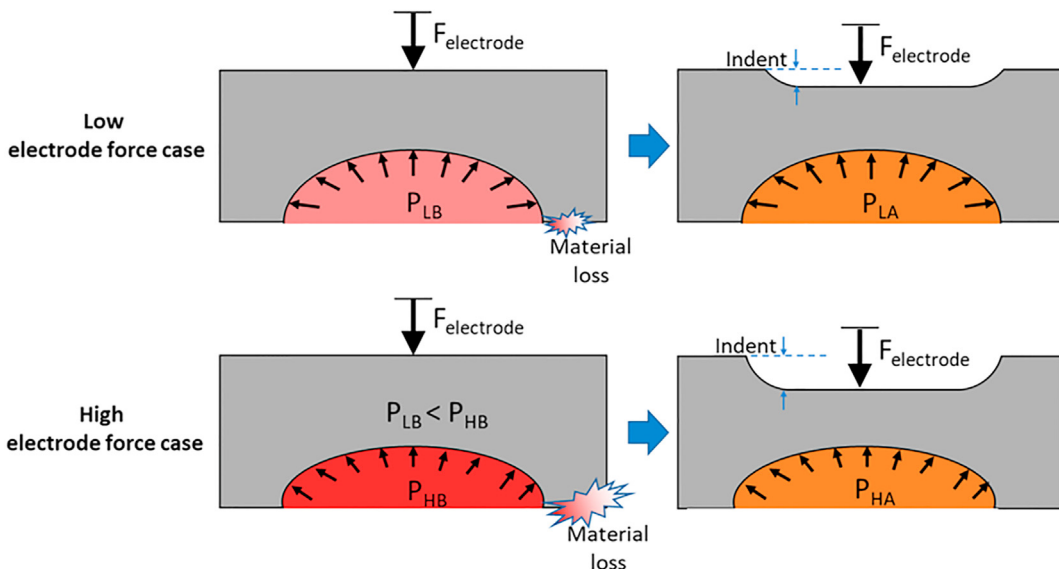


Fig. 11 – (a) Schematic showing a comparison of expulsion-free weld and weld with expulsion; (b) (c) (d) cross-sectional weld images with the denotation of electrode indent depth at moderate heat input level with 4.4 kN, 4.9 kN, 5.4 kN electrode force, respectively.



**Fig. 12 – Schematic of expulsion at low and high electrode force conditions with high heat input.**

more material is lost in the expulsion at high force as compared to the expulsion at low force due to higher pressure of the liquid, resulting in a deeper indent. This hypothesis is in-line with the observations of electrode indent depth change with change in electrode force, as can be seen in Figs. 13 and 14c, showing that in welds that experience expulsion, higher force leads to significantly deeper electrode indents at the high heat input level.

By correlating LME cracking severity and electrode indent depth, two patterns may be distinguished. In welds without expulsion (at low heat input) electrode indent depth was low, and so was the LME cracking severity (Fig. 14a). The embedded figure in Fig. 14a resolved the data in a different scale to fit the trendline. Despite a significant (but small) increase of electrode indent depth between the welds made with electrode forces of 4.4 kN and 5.4 kN, no increase of LME cracking

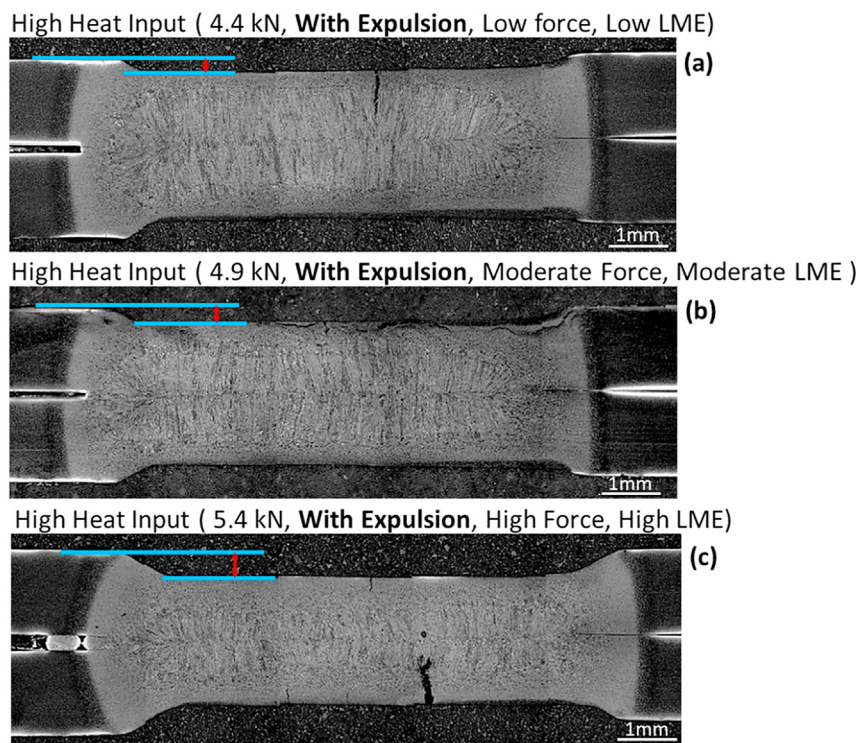


**Fig. 13 – Cross-sectional images of welds with expulsion at the high heat input level, (a), (b) and (c) with the electrode force of 4.4 kN, 4.9 kN, 5.4 kN, respectively.**

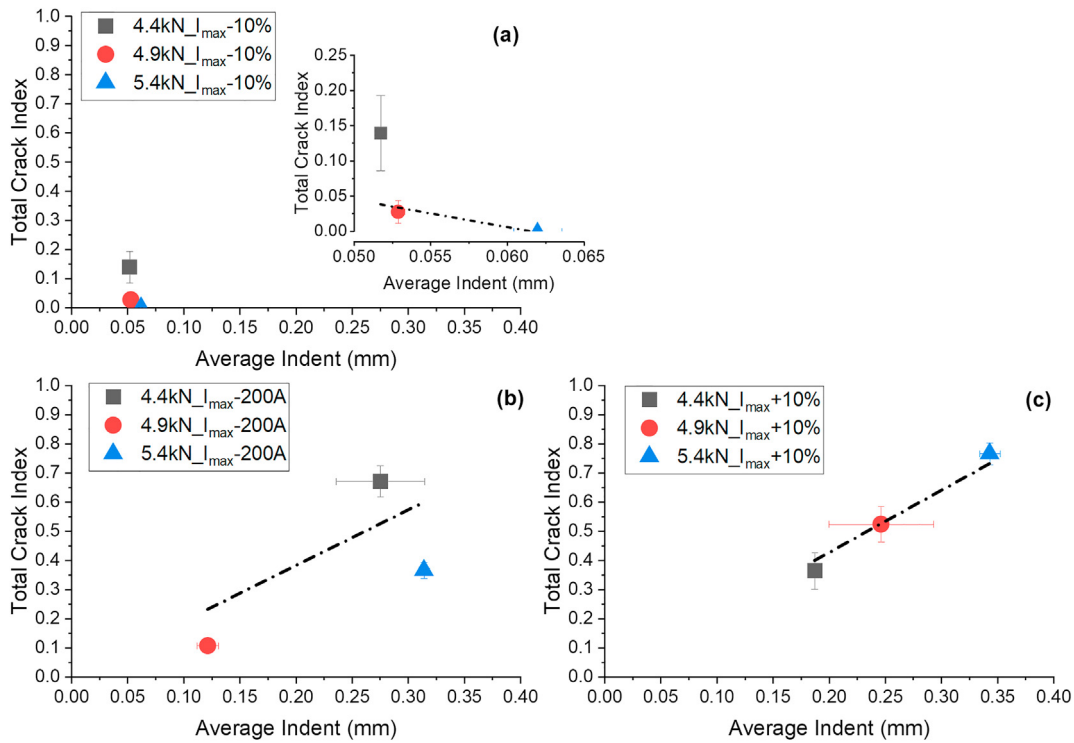


**Fig. 14 – Total crack index as a function of electrode force and average indent depth at (a) low; (b) moderate and (c) high heat input, respectively.**

severity was observed. Conversely, LME cracking severity decreased from a crack index of 0.14 for welds made with an electrode force of 4.4 kN to crack index of 0 for welds made with electrode force of 5.4 kN. In this case, higher heat extraction caused by higher electrode force was a predominant factor decreasing LME cracking severity, in-line with the observations from literature [12,13,15,17]. In welds with expulsion at high heat input (Fig. 14c), LME cracking severity increased linearly with indent depth. The same trend was also seen for welds made with moderate heat input (Fig. 14b). In the welds that experienced expulsion, higher electrode force led to deeper indent allowing more contact between the electrode and the sheet surface at the weld shoulder, which increased rapid cooling during electrode collapse leading to higher tensile stresses and more severe LME cracking.

#### 4. Conclusions

The automotive industry is currently researching resistance spot welding schedules that minimize the risk of LME cracking. This study investigated influence of electrode force on LME cracking of a high-LME susceptible material at the low (below expulsion limit), moderate (near expulsion limit) and high (above expulsion limit) welding heat input levels. Type B cracks were observed along with all three heat inputs levels while Type C cracks were absent. In addition, Type A cracks appeared at both moderate and high heat inputs. Multiple types and larger number of LME cracks were induced at higher

heat input levels. Crack index considering both crack length and frequencies drew an explicit conclusion for the LME cracking severity. When welds were made at low heat input, LME severity decreased from a Total CI of 0.14 to 0 when electrode force was increased from 4.4 kN to 5.4 kN. However, that same increase in electrode force resulted in an increase in LME (Total CI increased from 0.36 to 0.77) when welds were made at high heat input. When moderate heat input was applied, the Total CI decreased from 0.67 to 0.11 when electrode force was increased from 4.4 kN to 4.9 kN and then the Total CI increased to 0.37 when the electrode force was further increased to 5.4 kN. The observations showed that the severity of LME cracking did not always decrease with the increase of electrode force. The decrease of LME cracking with an increase of electrode force only was observed at low heat input where expulsion did not occur. At moderate heat input, the welds with expulsion possessed higher LME cracking than expulsion-free welds, deviating from the trend seen in the welds made with low heat input. At high heat input, expulsion happened at all electrode force conditions and the severity of LME cracking increased with increased electrode force. LME cracking was dominated by heat extraction at low heat input. At moderate heat input conditions where both expulsion and non-expulsion conditions were seen, LME was both heat transfer and collapse controlled. Finally, in welds made with high heat input, LME cracking was dominated by electrode collapse. However, it is obvious welds experiencing expulsion the electrode collapse had a much stronger effect controlling LME than did heat loss during the welding cycle. As regards as

the correlation of electrode indent depth and LME cracking severity, at low heat input, electrode indent depths and LME cracking were low and the increase of electrode force increased electrode indent but decreased LME cracking. At moderate heat input, welds with expulsion experienced deeper indent with more severe LME cracking. At high heat input, the increase of electrode force significantly increased electrode indent depth and LME cracking. In automotive assembly, expulsion often occurs during RSW. Under such circumstances, LME will be made more severe and its severity will increase with increased electrode force. Therefore, when using high electrode force to mitigate LME during welding, welding engineers must validate whether or not they are welding in expulsion conditions.

### Declaration of competing interest

The authors declare that they have no known competing financial interests or personal relationships that could have appeared to influence the work reported in this paper.

### Acknowledgments

This work was founded by the Auto/Steel Partnership (A/SP) as part of an Industrial welding solutions project that aims to improve RSW quality in 3G-AHSS. The authors would like to thank A/SP for the financial support.

### REFERENCES

- [1] ENVIRONMENTAL PROTECTION AGENCY 40 CFR parts 86 and 600 revised 2023 and later model year light-duty vehicle greenhouse gas emissions standards n.d.
- [2] Baluch N, Udin ZM, Abdullah CS. Advanced high strength steel in Auto industry: an overview. Eng Technol Appl Sci Res 2014;4:686–9. <https://doi.org/10.48084/ETASR.444>.
- [3] Sah SK, Bawase MA, Saraf MR. Light-weight materials and their automotive applications. SAE Tech Pap 2014;4. <https://doi.org/10.4271/2014-28-0025>.
- [4] Tisza M. Three generations of advanced high strength steels in the automotive industry. Lect Notes Mech Eng 2021;22:81–94. [https://doi.org/10.1007/978-981-15-9529-5\\_7](https://doi.org/10.1007/978-981-15-9529-5_7).
- [5] Marder AR. The metallurgy of zinc-coated steel. Prog Mater Sci 2000;45:191–271. [https://doi.org/10.1016/S0079-6425\(98\)00006-1](https://doi.org/10.1016/S0079-6425(98)00006-1).
- [6] Kimchi M, Phillips DH (Welding instructor). Resistance spot welding : fundamentals and applications for the automotive industry n.d.:115.
- [7] Beal C, Kleber X, Fabregue D, Bouzekri M. Liquid zinc embrittlement of twinning-induced plasticity steel. Scripta Mater 2012;66:1030–3. <https://doi.org/10.1016/j.scriptamat.2011.12.040>.
- [8] DiGiovanni C, He L, Pistek U, Goodwin F, Biro E, Zhou NY. Role of spot weld electrode geometry on liquid metal embrittlement crack development. J Manuf Process 2020;49:1–9. <https://doi.org/10.1016/j.jmapro.2019.11.015>.
- [9] Böhne C, Meschut G, Biegler M, Frei J, Rethmeier M. Prevention of liquid metal embrittlement cracks in resistance spot welds by adaption of electrode geometry. Sci Technol Weld Join 2020;25:303–10. <https://doi.org/10.1080/13621718.2019.1693731>.
- [10] Murugan SP, Mahmud K, Ji C, Jo I, Park Y Do. Critical design parameters of the electrode for liquid metal embrittlement cracking in resistance spot welding. Weld World 2019;63:1613–32. <https://doi.org/10.1007/s40194-019-00797-y>.
- [11] Dupuy T. A novel electrode tip geometry to mitigate liquid metal embrittlement during resistance spot welding. Weld World 2022;66:1715–31. <https://doi.org/10.1007/s40194-022-01343-z>.
- [12] Choi DY, Sharma A, Uhm SH, Jung JP. Liquid metal embrittlement of resistance spot welded 1180 TRIP steel: effect of electrode force on cracking behavior. Met Mater Int 2019;25:219–28. <https://doi.org/10.1007/s12540-018-0180-x>.
- [13] Kim YG, Kim IJ, Kim JS, Chung Y Il, Choi DY. Evaluation of surface crack in resistance spot welds of zn-coated steel. Mater Trans 2014;55:171–5. <https://doi.org/10.2320/matertrans.M2013244>.
- [14] Siar O, Dancette S, Dupuy T, Fabrègue D. Impact of liquid metal embrittlement inner cracks on the mechanical behavior of 3rd generation advanced high strength steel spot welds. J Mater Res Technol 2021;15:6678–89. <https://doi.org/10.1016/j.jmrt.2021.11.100>.
- [15] Barthelme J, Schram A, Wesling V. Liquid metal embrittlement in resistance spot welding and hot tensile tests of surface-refined TWIP steels. IOP Conf Ser Mater Sci Eng 2016;118:012002. <https://doi.org/10.1088/1757-899X/118/1/012002>.
- [16] Meschut G, Böhne C, Rethmeier M, Biegler M, Frei J. AHSS implementation solutions - LME program. Brussels, Belgium: 2020.
- [17] DiGiovanni C, He L, Pan H, Zhou NY, Biro E. Predicting liquid metal embrittlement severity in resistance spot welding using hot tensile testing data. Weld World 2022;66:1705–14. <https://doi.org/10.1007/s40194-022-01320-6>.
- [18] Wintjes E, DiGiovanni C, He L, Bag S, Goodwin F, Biro E, et al. Effect of multiple pulse resistance spot welding schedules on liquid metal embrittlement severity. J Manuf Sci Eng 2019;141:1–9. <https://doi.org/10.1115/1.4044099>.
- [19] DiGiovanni C, Bag S, Mehling C, Choi KW, Macwan A, Biro E, et al. Reduction in liquid metal embrittlement cracking using weld current ramping. Weld World 2019;63:1583–91. <https://doi.org/10.1007/s40194-019-00790-5>.
- [20] Wohner M, Mitzschke N, Jüttner S. Resistance spot welding with variable electrode force—development and benefit of a force profile to extend the weldability of 22MnB5+AS150. Weld World 2021;65:105–17. <https://doi.org/10.1007/s40194-020-01001-2>.
- [21] Ashiri R, Shamanian M, Salimjazi HR, Haque MA, Bae JH, Ji CW, et al. Liquid metal embrittlement-free welds of Zn-coated twinning induced plasticity steels. Scripta Mater 2016;114:41–7.
- [22] Böhne C, Meschut G, Biegler M, Rethmeier M. Avoidance of liquid metal embrittlement during resistance spot welding by heat input dependent hold time adaption. Sci Technol Weld Join 2020;25:617–24. <https://doi.org/10.1080/13621718.2020.1795585>.
- [23] Kasuya T, Yurioka N. Carbon equivalent and multiplying factor for hardenability of steel n.d.
- [24] American Welding Society. AWS d8.9:2012 test methods for evaluating the resistance spot welding behavior of automotive sheet steel materials. Miami, FL: American Welding Society; 2012.
- [25] Ghatei-Kalashami A, Ghassemali E, DiGiovanni C, Goodwin F, Zhou NY. Occurrence of liquid-metal-embrittlement in a fully ferritic microstructure. Materialia 2021;15:101036. <https://doi.org/10.1016/j.mtla.2021.101036>.

- [26] DiGiovanni C, He L, Hawkins C, Zhou NY, Biro E. Significance of cutting plane in liquid metal embrittlement severity quantification. *SN Appl Sci* 2021;3. <https://doi.org/10.1007/s42452-021-04608-2>.
- [27] Wintjes E, DiGiovanni C, He L, Biro E, Zhou YN. Quantifying the link between crack distribution and resistance spot weld strength reduction in liquid metal embrittlement susceptible steels. *Weld World* 2019;63:807–14. <https://doi.org/10.1007/s40194-019-00712-5>.
- [28] Midawi ARH, Barber B, Pearson K, Sherepenko O. Comparative analysis of liquid metal embrittlement reduction methods in zinc-coated gen3-AHSS n.d.
- [29] Böhne C, Meschut G, Biegler M, Rethmeier M. The influence of electrode indentation rate on LME formation during RSW. *Weld J* 2022;101:197–207. <https://doi.org/10.29391/2022.101.015>.